General Remarks

We thank both reviewers for their time and the constructive comments, which will improve the quality of the paper. The referee comments are formatted in grey and our response in black with indentation and numbering (R##). The line and figure numbers refer to the revised version.

Specific Reply to Referee #1

The paper by Radenz et al. introduces an effective and user-oriented way to present height-resolved transport modelling simulations associated with aerosol sources. Moreover, the methodology can be applied independently of observations and can be tuned to accommodate unusual aerosol emissions such as volcanic eruptions or intensive biomass burning episodes. The results highlight the robustness and usefulness of the technique when compared against advanced lidar data. Nevertheless, the presentation of the methodology and results should be improved to help the reader understand the ramifications of the study. Moreover, the precision of the language could be improved. There are several issues and technical comments that can improve it. The paper can be published in ACP although it does not fit yet the scope of the Special Issue (EARLINET aerosol profiling: contributions to atmospheric and climate research). The authors should consider to acknowledge EARLINET if they want to keep the link with this Special Issue given that Polly instruments also participate in the network. In the following, comments are given for consideration in Specific Comments. The last section lists the Technical Comments.

R1: We are now highlighting the contribution of EARLINET to the improvement of the Polly systems in the acknowledgements. Furthermore, we added EARLINET as a potential use case into the discussion.

Specific Comments

Ln2 & Ln51: I understand that the distinction “backward trajectories or particle positions" refer to Hysplit and Flexpart respectively. However, in line 51 you refer to “backward trajectories" for the two models. Therefore, I ask you to clarify throughout the text and keep homogeneous wording to avoid confusion.

R2: Thanks for raising that inconsistency. We decided to settle on air parcel position for a single particle position or point in a backward trajectory.

Ln8 & Ln59: Is it 7- or 8-week campaigns? Please correct.

R3: We settled for ‘multi-week’ in the abstract and introduction. The durations are quantified in Section 3.

§1: In the introduction, you describe that trajectory models simulate air parcels while particle dispersion models simulate particles. In my understanding, the terms “airmass" and “air" include the terms above. It would be nice to clarify this in the text.

R4: From our understanding, an air parcel is an infinitesimally small volume of air, whereas an airmass is a larger volume of air with consistent properties (e.g. composition, origin, aerosol load, moisture content). We added a sentence clarifying this.

Ln20–21: Please give the abbreviations and anywhere else.

R5: As all these abbreviations refer to well-known models and each is cited with a reference, we see no additional benefit of expanding them. We consider this usage covered by the Copernicus house standards:

"Abbreviations: […] In order to avoid ambiguity, abbreviations that could have numerous meanings must be defined (e.g. "GCM" could stand for "global climate model" or "general circulation model"). This generally does not apply to abbreviations that are better known than their written-out form (e.g. NASA, GPS, GIS, MODIS)."
We expanded the GDAS1 abbreviation.

§2: A summary table with the versions of the models, the meteorological data, the pros and cons, etc. will enhance the clarity of this section.

R6: As meteorological input both models basically use the GFS analysis, however due to technical reasons in two different formats (GDAS as ARL binary and GFS analysis as grib). The FLEXPART version is already mentioned in the text.
We consider a comprehensive discussion of the difference between trajectory models and Lagrangian particle dispersion models beyond the scope of this publication. Please note, that the HYSPLIT model also contains a module for particle simulations, though with a less sophisticated treatment of turbulence.

Figure 1: A similar Figure for Flexpart is needed.

R7: We added a respective subfigure to Fig. 1. But please note that only a fraction of the particle positions could be shown. Also suggested by referee #2, please refer to R36.

Ln70: What is a "wind trajectory"? I am confused. Hysplit and Flexpart rely on meteorological data to drive the simulations.

R8: The term 'mean wind trajectory' was used to emphasize the non-turbulent nature of the transport calculation, see Stohl (2002).

Ln83: What does it mean "purpose-serving"? Could you expand on this?

R9: Too small areas cause fuzzy statistics of residence time. We replaced 'purpose-serving' by 'robust'.

Figure 2 & Figure 3: Both Figures are not introduced and explained in the manuscript!

R10: Both references were added.

Figure 3: Figures 3a, 3b, and 3c refer to Limassol, Punta Arenas, and the shipborne observations, respectively. What are the figures for Krauthausen and Finokalia of Section 5?

R11: For Finokalia and Krauthausen also Fig. 3 (a) is used. This becomes clear by the categories shown in Fig. 13 and 14 (14 and 15 in revised version). However, we added this explicitly in the text.

Why the geographical areas are not uniformly defined? Why the Oceans are not included in this selection? What is the reason behind this decision?

R12: We are not sure what is meant with 'uniformly distributed'. The whole globe is not covered by polygons, because the intent is to specifically test how much residence time can be attributed to the most probable sources. For example, long-range transport across the innertropical convergence zone is rare, hence including southern hemispheric sources to the analysis of the European site would only clutter the statistics, without adding information. Global coverage of the globe is provided by the land surface mask.
Oceans are not included in the geography version, because they are covered with the water surface property of the land surface classification. Aerosol emission by oceans is too transient in it's nature to be attributed to static regions. E.g. it depends of wave

characteristics (height and breaking/non-breaking waves, which is driven by wind speed, ocean currents and seafloor topography) and marine productivity.

Ln94–97: The residence times for Flexpart and Hysplit are not comparable. Could they be normalized?

R13: Yes via the formula given in Eq. 1. To avoid further confusion, we decided to normalize the residence time shown in the comparison. Figures 1 b,d, 5, 9 and 12 (revised version 1 b,d, 6, 10, 13) were updated accordingly. Also suggested by referee #2, please see R34.

Pg6Ln106–107: Although Baars et al. (2017) provide the information, a brief description for retrieving the high resolution products should be introduced with the aim to make the manuscript self-contained.

R14: We added a description of the quasi particle backscatter to Sec. 3.

§4.1: It would be nice to see the values of the intensive parameters that characterize the aerosol layers similar to §4.2.

R15: Was added as new Fig. 5. A similar point was raised by referee #2, please refer to R32.

Ln146–149: Could it be that the airmass, although originated from N. America, is aerosol-free over the measuring site? Is it safe to make this assumption? Polly a high-performance lidar and it should be used to demonstrate the validity of the methodology. I consider that increasing the averaging either temporally or vertically or both will demonstrate if something resides in higher altitudes.

R16: Yes, as we state in the manuscript (now lines 278-279), residence time over a certain surface is only a necessary, not a sufficient condition for aerosol load to be present. For example, the wind speeds at the source location could not have be sufficient for dust mobilization or the soil was too moist.

Figure 4 & Figure 6 & Figure 10: For the sake of completeness, you could report the particle backscatter coefficient for the “orange" sectors? Also, Baars et al. (2017) produce target classification maps that I consider valuable for the assessment of the overall performance of the methodology.

R17: The orange bars mark the period of the manual analysis. The respective backscatter is shown in the leftmost panel of Fig. 7, 8 and 11 (revised version 8, 9, 12).
We consider including the target classification beyond the scope of this study, as the classification is distinctively different to aerosol typing and would not provide any new information. However, we agree, that the combination of airmass source attribution and the classification or an aerosol typing is an interesting topic for future work. We state this now in the outlook section (now lines 306-207).

Ln143–144 & Figure 5: What could be the reason that the last 0.5-1 km of the aerosol layer remain undetected? The same is visible for Figure 9.

R18: (Now lines 160-161 and Fig. 6) In both cases this issue is likely caused by insufficiencies of the meteorological fields used as an input. One could speculate, that the dust load itself changed the dynamics, i.e. by heating the layer and causing lifting. Those effects are not well represented in the analysis used as input for the transport simulations.
For the Punta Arenas case (now Fig. 10), the backscatter plot and the airmass source estimate agree on the top being at 6km.

Ln163–166: What is the origin of this layers? The signature of this layer is somewhat different from a dust layer.

R19: The origin of the layers above 2.5 km during the morning period is hard to pinpoint. The airmass source estimate (and thus the model meteorology) suggest barren surface and

Sahara as the sources. But the optical properties (now Fig. 9) and the temporal evolution (now Fig. 7), indicate the leading edge of the Middle East plume (see R20 below). As HYSPLIT and FLEXPART agree quite well, the source for this disagreement is not the transport simulation, but likely the meteorological input fields. This is already noted in the section on the source attribution "While the general transition was captured by the source estimate, the leading edge of the 'Arabian Peninsula' plume was observed over Limassol earlier than indicated." (line 175-176, now lines 195-196).
The time-height plot of depolarization ratio (now Fig. 7b) suggests that the dust fraction of the mixture increased only at 03:30 UTC, causing inhomogeneities over the averaging period. But as the focus of this profile is the lower layer, clearly being attributed to Saharan airmasses we would like to stick to this averaging period. We expanded the section to include this discussion.

Ln169–170: Is it a mixed dust layer? Is Middle East dust mixed with anthropogenic particles? Can you clarify?

R20: Yes, we consider this layer being dust mixed with anthropogenic pollution, due particle depolarization ratio, which is lower than would be expected for pure dust. A contribution of absorbing particles of anthropogenic origin is plausible, given industrial areas in the Middle East.

Figure 10: What are the dense backscattering features (e.g., around 4-5 km at 12utc)? Is it because of the color scale or are they clouds? If they are clouds, shouldn't they be removed?

R21: (Now Fig. 11). The mentioned features are boundary layer clouds. As Figure 11 is supposed to provide an overview of the measurement scene we decided to keep all features in. We added a sentence to the descriptions (now lines 207-210). See also R33.

Figure 12 (a & b): It seems that the profiles indicate "Water" from the ground up to 10km. This finding is in disagreement with the lidar data. How should we treat this?

R22: (Now Fig. 13). Generally open oceans are a weak aerosol source, especially for the free troposphere. We thus do not see an inconsistency here, e.g. Bourgeois et al. (2018, ACP) and Murphy et al. (2019, ACP)

Figure 13: Similarly, the simulations indicate significant aerosol transport over 6 km, whereas the lidar suggests otherwise.

R23: (Now Fig. 14). As mentioned in the paper, the lidar undersampled periods with high residence times over barren ground and Europe/Sahara respectively by a factor of up to 10 (now lines 252-255). Such an undersampling happens, if certain transport regimes are correlated with low level cloud cover or other conditions inappropriate for lidar observations, for which no optical properties can be retrieved. We nevertheless added a sentence to clarify that point.

Technical Comments

[…]

R24: We considered all the technical comments in the revised version of the manuscript, but decided not to quote the list in the response. Thanks for your effort of pointing them out.

Specific Reply to Referee #2

Characterization of atmospheric aerosols using ground based lidar measurements de-pend upon accurate attribution of the sources of the aerosol. Often this is achieved by selecting specific altitudes and times representing interesting features in the lidar pro-files and then running back trajectories from those locations. This paper describes a method to do this in a continuous way by using ensemble trajectories from the HYSPLIT or particle dispersion modelling from FLEXPART. The authors had presented elements of this methodology in earlier publications and have now presented them in a consoledated way. They give examples showing the application of the methodology as well as give an assessment of the representativeness of time limited ground based lidar observations. This is an interesting paper and may have ramifications for other applications.

The basic contents of the manuscript are clear. However the presentation suffers from many typos, grammar and English usage issues. The paper is well within the scope of ACP and will be useful to the remote sensing community. I recommend publication after some revisions. Here are my comments/suggestions in no particular order:

1. While the paper is geared towards the ground based lidar observations, I am wondering if the methodology can be adapted for global spaceborne observations by say CALIPSO and other forthcoming lidars. If the sources of, say the dust layers observed at a remote location by CALIPSO could be reliably and continuously attributed in an automated way, then as a first approximation, one may be able to assign the lidar ratios corresponding to those sources which are known to vary significantly. Similarly, it is conceivable that variable lidar ratios may be assigned to the ageing smoke layers using this method. Using variable lidar ratios in this way should improve the extinction products from elastic lidars like CALIPSO. It will be good if the authors could discuss the feasibility of this scenario, which would add to the value of the paper.

R25: Thanks for pointing out this aspect. We added a brief paragraph into the discussion (lines 298-303).

2. I think it will be nice to have validation of some of the results presented. For in-stance, in Figures 10-12 the authors analyze an aerosol blob between 2-6 km which is estimated to be originating from Australia. From the retrieved lidar ratios and depolarization ratios, it appears that the layer is likely to be lofted smoke. However, it would be good to provide evidence of fire events in Australia around 15-20 May 2019. Do CALIPSO transects close to Punta Arenas on May 20, 2019 show any lofted smokelayer? In Figure 11, The lidar ratio at 532 nm between 2-3 km is about 50 sr and below1 km is even higher. Would the authors comment on these. There are also some differences between the HYSPLIT and FLEXPART simulations for this case (Figure 12cand 12d).

R26: There were various wildfires in southwestern Australia from the 13 to 16 May. A map combining MODIS fire radiative power and an ensemble trajectory was added to the appendix (Fig. A1). Fires in the central part of Chile (Bio Bio province, 1700 km north of Punta Arenas) during the same period were not touched by any trajectory. We checked the CALIPSO overpasses intersecting the backward simulation within 200km and 2 hours from the 15 to the 20 May, but could not find any similar plumes. The areas of interest were frequently covered by cirrus clouds. The high lidar ratio below 1km was caused by a deajustment of the 607 near-range channel. We decided to omit the near-range extinction and lidar ratio in that figure (now Fig. 12).

Perhaps a better example would be transported plumes from Australian fire events in January 2020—as described in Ohneiser et al. (2020, ACP, 20, 8003).

R27: We do not consider the Ohneiser 2020 a useful example to validate our method. Transport processes across the tropopause are not well captured in the used meteorological data and

the model physics. As can be seen in their Fig. 2., the reception height would have to been set to 20km to include the pyroCB lifting. Such a high reception height degrades the selectivity of the residence times and makes those instances harder to interpret.

3. Why not give the altitude scale in Figures 4, 6 and 10 in km as in the other plots for uniformity? Also the plots for the lidar data and residence time profiles may be shown up to the same altitude for easier comparison.

R28: Thanks for pointing out this inconsistency; we decided to settle on 8km as top for the plots related to the case studies. The height unit of the quasi particle backscatter plots (now Fig. 4, 7 and 11) is now km.

4. I think some sort of sensitivity study will be useful, e.g. running the trajectories for different number of days and checking if this leads to any difference in the results. Similarly, does varying the number of trajectories improve the difference between the HYSPLIT and FLEXPART results discussed (line 135-136) in relation to Figure 5 or Figure 12?

R29: A sensitivity study would require extending the manuscript significantly while, in our opinion, the added information would not justify this expansion. The comparison of FLEXPART to HYSPLIT for each case gives an impression of the variability to be expected from different number of air parcels. A more rigorous sensitivity analysis would require the development of a skill metric and longer-term transport simulations with different settings. Generally, the required number of air parcels is related to the area of the source that should be attributed. To captures point sources, e.g. release of radioactive substances or inert chemical tracers, correctly, a several thousands of air parcels are required. When larger areas are the potential sources, such as dust mobilization, a couple of hundred to a few thousand particles are usually sufficient to capture emission and transport.

5. Adding location maps showing the points of observation will add context to the Figures.

R30: We think that adding further figures or subfigures would expand the article too much. Detailed information on the setting of each measurement site is provided in the original literature. However, we added markers to the overview maps in Fig. 3 so that the reader can get an overview in the beginning.

6. Adding the corresponding depolarization plot for Figure 4 will be helpful.

R31: The volume depolarization ratio plot was added for the Polarstern and Limassol case (now Fig. 4b and 7b).

7. I am a little confused about the features at the lowest altitudes in the lidar observations. For instance in Figure 4, the highest backscatter values occur at the lowest altitudes below 1 km. Firstly, for the sake of completeness, I think it would be better to reproduce the Yin et al. (2019) Figure 14, instead of the reader having to go back to that paper or better still, present the manual analysis for another segment (and include the profile of lidar ratios in that plot).

R32: We added the optical profiles analyzed with the Raman method between 22 and 23 UTC (new Fig 5).

As mentioned in Yin et al. (2019), the extinction coefficients within the MBL are too large to be entirely from the marine aerosols. Could these really be explained by the pollution coming from Europe with their relatively small contribution to the residence times? Similarly, in Figure 10, very high backscatter can be seen between 14-18 UTC around 1.5 km, but the authors do not mention this in the discussion. Is this a measurement artifact? Similar high backscatter blobs can also be seen between 4-8 km at different times in this Figure.

R33: (Now Fig 11). In both cases these features are clouds and aerosol particles subject to strong hydroscopic growth. We added a sentence in the description of the case (lines 142-143 and 206-208). Please also refer to R21.

8. Add unit of accumulated residence time in Figure 1b. The accumulated residence times from HYSPLIT and FLEXPART are very different in Figures 5, 9 and 12 and creates confusion for comparison. The reason for this should be clarified in the text.

R34: This issue is connected to a similar comment by Referee #1, please refer to R13.

9. Define NR in legends to the lidar Figures.

R35: The abbreviations now described in the figure captions.

10. For completeness it would be good to include an example of the FLEXPART simulations.

R36: Also suggested by referee #1, please refer to R7.

Automated time-height-resolved airmass source attribution for profiling remote sensing applications

Martin Radenz[1], Patric Seifert[1], Holger Baars[1], Athena Augusta Floutsi[1], Zhenping Yin[1,2,3], and Johannes Bühl[1]

[1]Leibniz Institute for Tropospheric Research (TROPOS), Leipzig, Germany
[2]School of Electronic Information, Wuhan University, Wuhan, China
[3]Key Laboratory of Geospace Environment and Geodesy, Ministry of Education, Wuhan, China

Correspondence: Martin Radenz (radenz@tropos.de)

Abstract. Height resolved airmass source attribution is crucial for the evaluation of profiling ground-based remote sensing observations. This work presents an approach of how backward trajectories or particle positions from a dispersion model can be combined with geographical information (a land cover classification and manually defined areas) to obtain a continuous and vertically resolved estimate of airmass source above a certain location. Ideally, such an estimate depends on as few as possible a-priori information and auxiliary data. An automated framework for the computation of such an airmass source is presented and two ~~exemplary~~ applications are described. Firstly, the airmass source information is used for the interpretation of airmass sources for three case studies with lidar observations from Limassol (Cyprus), Punta Arenas (Chile) and ship-borne off Cabo Verde. Secondly, airmass source statistics are calculated for two ~~8-week~~ multi-week campaigns to assess potential observation biases of lidar-based aerosol statistics.

1 Introduction

Tracing airmass transport ~~trough~~ through a turbulent atmosphere is (still) a complex ~~and entangled~~ problem. Especially the transport of aerosols and consequently the ~~interaction~~ interactions with clouds, precipitation and radiation ~~require~~ are required to capture the four-dimensional history of an air parcel. When it comes to practical application, such as the analysis of aerosol observations or aerosol-cloud interaction studies, the ease of interpretation is often hindered by the amount of data that needs to be considered.

Models that simulate airmass transport can be broadly grouped into trajectory models and particle dispersion models (overview provided by Fleming et al., 2012). Trajectory models calculate the transport of a single air parcel imposed by the mean meteorological fields. The model simulations can be ~~either run~~ run either forward or backward in time, providing information about ~~either the source or~~ the source and the destination of the airmass, respectively, after a given transport time. Turbulence and vertical motion during the transport ~~process are usually parametrized~~ are usually parameterized on the grid

scale. Commonly used models are HYSPLIT (Stein et al., 2015), FLEXTRA (Stohl et al., 1995) and LAGRANTO (Wernli and Davies, 1997; Tarasova et al., 2009). Due to the rather simple approach, the results are quite uncertain (Seibert, 1993; Polissar et al., 1999), but computational requirements are comparably low. A straightforward approach to represent some of the variability is to calculate spatial or temporal ensembles of the trajectories (Merrill et al., 1985; Kahl, 1993; Draxler, 2003). Lagrangian particle dispersion models (LPDM) with a large number of particles are set up to cover turbulent and diffusive transport even more realistically (Stohl et al., 2002). The fate of each particle is tracked individually, allowing more variability to be included into the transport simulation. A frequently used LPDM is FLEXPART (Pisso et al., 2019).

Generally, representation of chaotic motion in the atmosphere improves with larger ensembles of trajectories or increasing number of particles. But, with dozens to hundreds ~~airmass locations available~~of air parcel locations available, interpretation rapidly becomes cumbersome. A number of infinitesimally small air parcels grouped together gives an airmass, a larger volume of air with similar properties. Residence times are a well established technique for attributing regional information to airmass properties such as being laden with aerosols, moisture or trace gases (Ashbaugh, 1983; Ashbaugh et al., 1985). ~~Using backward transport simulations~~

Using backward simulations of air parcel positions, analysis of the residence time yields useful information about the potential source region of an observed airmass. The basic assumption is, that the longer an air parcel was present in a certain region, the more likely it will be influenced by the surface characteristics. Hence, the dimensionality of an air parcels 4D location can be reduced to the residence time. Approaches for clustering backward trajectories by direction, source regions or latitude ~~is widely done. Most available approaches~~ are widely used. The majority focus on the interpretation of timeseries observations at single heights - mostly close to ground (e.g. Escudero et al., 2011), for aircraft intersects (e.g. Paris et al., 2010) or over a whole region (Lu et al., 2012). More sophisticated approaches blend the residence time with actual concentration measurements (Stohl, 1996; Heintzenberg et al., 2013). However, these approaches require continuous concentration time series, which are generally not available for remote sensing observations. Furthermore any profile information above the measurement site is neglected.

When interpreting ground-based remote sensing observations the airmass sources are ~~attributed by manually selecting~~ assigned by manually selected periods (time and height above ground), that seem interesting for further investigation and calculating backward transport for that specific cases. For example optical properties of aerosol layers retrieved from lidar observations are frequently connected to airmass sources (e.g., Müller et al., 2007; Mattis et al., 2008). If airmass source estimates are required for longer time periods or multiple heights, calculating, visualizing and interpreting the results ~~becomes~~ become tedious. Hence, a continuous, computationally efficient, easy to interpret and automated airmass source estimate is required. To be broadly and easily applicable, such a source estimate should not require extensive a-priori information, such as clusters of trajectories or potential source contribution functions. The required approach is intended to be also simpler than using a coupled aerosol model, such as CAMS (Flemming et al., 2017), COSMO-MUSCAT (Dipu et al., 2017) or ICON-ART (Rieger et al., 2015). ~~Though~~ Although these models can provide profiles of atmospheric composition, they usually do not provide information on the source.

In hereHerein, we propose a combination of automated backward trajectory calculations and geographical information for the setup of a simple, spatio-temporally resolved airmass source attribution scheme. As a proxy for geographical information, two products are used: a land cover classification mask and manually defined geographical areas. The methodology is described in the following section 2. An A comprehensive, easy to use software package is also provided. Earlier versions were already used in Haarig et al. (2017), Foth et al. (2019) and Floutsi et al. (2020). Afterwards two applications illustrate potential use cases. In the first example, the temporal and vertical evolution of the airmass source is analyzed for three lidar observations of different aerosol conditions from Limassol (Cyprus), Punta Arenas (Chile) and on board R/V Polarstern off Cabo Verde. In the second application example, vertically resolved airmass source statistics are used to assess potential observation biases of long-term lidar-based aerosol statistics. Two 7-week campaigns out multi-week campaigns of the PollyNET dataset (Baars et al., 2016) are presented: Finokalia (Greece) and Krauthausen (Germany).

2 Airmass source attribution method

In a conceptualized view, properties of an air parcel arriving over a location of interest are characterized by a certain surface type, if the air was close to the surface during its pasttravelled path. The 'proximity' to the surface can be parameterized as a reception height, which depends on the mixing state of the atmosphere at this location as well as on the type of aerosol particles that could be potentially potentially be emitted (i.e. mineral dust or sea salt). Conceivable choices for the reception height are the model-derived depth of the atmospheric boundary layer or fixed thresholds. As a first estimate for identification of possible surface effects on an air parcel, $2\,\mathrm{km}$ is widely used (Val Martin et al., 2018). It is assumed that, the more time an air parcel resides close to the surface, the more likely it acquires will acquire the aerosol footprint of the surface. The residence time - the total time an air parcel spend spent over a certain surface and below the reception height - is a first hint for the aerosol characteristics of the air parcel.

The transport pathway of an airmass arriving over the site can be computed either using mean wind using either mean-wind trajectories or a particle dispersion model. Both approaches can be used with the proposed method method proposed in this study. Mean wind trajectories for the past 10 days are calculated using HYSPLIT (Stein et al., 2015). To account for variability, ensemble trajectories consisting of 27 members, spaced $0.3°$ horizontally and $220\,\mathrm{m}$ vertically around the end point, are used (Fig. 1 a). Meteorological input data for HYSPLIT are taken from the GDAS1 dataset (obtained from the Global Data Assimilation System dataset at $1°$ horizontal resolution (GDAS1) provided by the Air Resources Laboratory (ARL) of the U.S. National Weather Service's National Centers for Environmental Prediction (ARL Archive). The location of the air parcel is stored in steps of 1 hour steps. A more realistic representation of turbulence and mixing can be achieved using a LPDM, which simulates the pathway of hundreds to thousands of particles. Here the most recent version of FLEXPART (Stohl et al., 2005; Pisso et al., 2019) is used. Meteorological data is obtained from the GFS analysis at a horizontal resolution of $1°$ (NOAA, 2000). 5000 500 particles are used with the particle positions being stored every 3 hours. These simulations are run every 3 hours with height steps of $500\,\mathrm{m}$ for the whole period of interest.

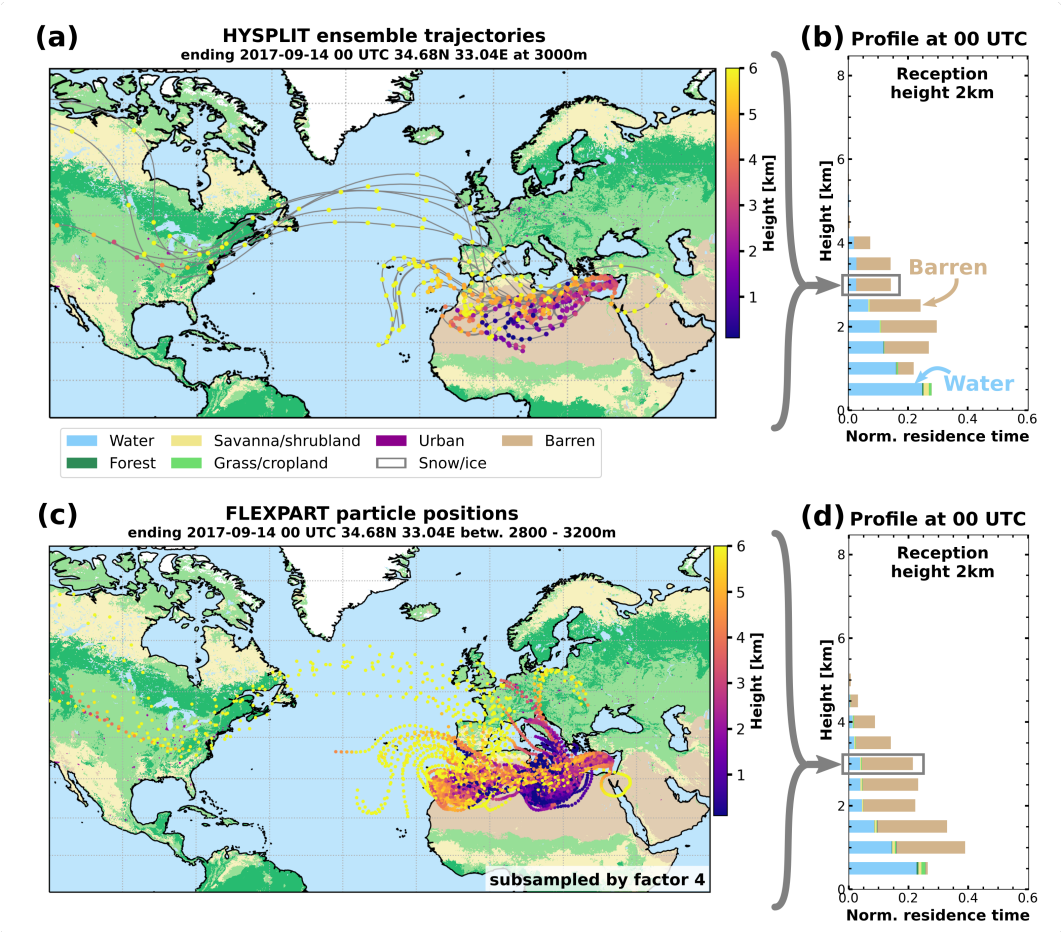

Figure 1. Example of how the residence time profile is calculated. HYSPLIT ensemble backward trajectories (a) and FLEXPART particle positions (c) ending ~~at~~ above Limassol on the 14 September 2017 00 UTC at 3 km height~~(~~. The number of FLEXPART particles is reduced by a factor of 4 in this visualization (i.e. 10000 instead of 40000)~~are used to calculate~~ . A time-resolved version with all particles is provided in the ~~profile of residence times per~~ supplement. Air parcel height is color-coded. The simplified MODIS land surface ~~class~~ classification (Fig. 2) is shown in the background. The profiles of normalized residence time with a reception height threshold of 2 km for HYSPLIT ensemble trajectories (b) and FLEXPART particle positions (d) are shown.

In this work, surface is classified by two methods: (1) a simplified version of the MODIS land cover classification (Friedl et al., 2002; Broxton et al., 2014). The 17 categories of the original dataset are grouped ~~to~~ into 7 categories according to Tab. 1 in order to allow for ~~purpose-serving~~ robust statistics in the output (Fig. 2). Additionally, the horizontal resolution is reduced to $0.1°$. The categories do not resolve the annual cycles, for example due to growing seasons. (2) customly defined areas as polygons, named according to their geographical context (Fig. 3). These areas can be tailored to the measurement location and/or scientific interest.

MODIS Category	Simplified Category
0	water
1, 2, 3, 4, 5, 6	forest
7, 8, 9	savanna/shrubland
10, 11, 12, 14	grass-, cropland
13	urban
15	snow
16	barren

Table 1. Overview ~~,~~ of how the MODIS land surface categories translate into the simplified categories used in this study. MODIS Category numbers as in (Broxton et al., 2014)

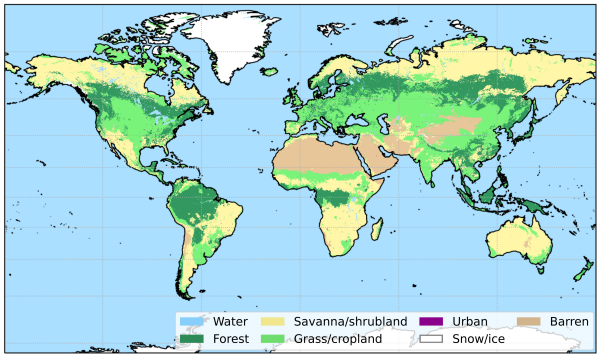

Figure 2. The simplified MODIS land cover classification. Details are given in the text.

The residence times at each time and height step are summed for each land cover class or polygon, where the ~~backtrajectory or particle~~ air parcel was below the reception height. Within this study, the widely applicable reception height threshold of $2\,\mathrm{km}$ is used (Val Martin et al., 2018). Different settings can be easily applied to study events which are entrained at greater heights, such as wildfire smoke emission or volcanic eruptions. The vertical airmass transport during such events is usually not accurately covered by atmospheric models. Setting the reception height to the maximum emission height of such events (as can be estimated, e.g., from satellite observations) can bypass the uncertainties in the modeled vertical motion. The residence times for each category and each height can then be visualized as a profile (Fig. 1 b). Where the residence time is 0, no air parcels were observed below the reception height during the duration of the backward simulation. In the example shown in Fig. 1 (b) above $5\,\mathrm{km}$ height, no airmasses resided at heights below $2\,\mathrm{km}$ above ground in the prior 10 days. The theoretical maximum residence time in hours depends on the number of trajectories or particles n, the duration of backward calculation d in days and the interval of output Δo in hours:

$$t_{\mathrm{max}} = n\,d\,\frac{24}{\Delta o} \tag{1}$$

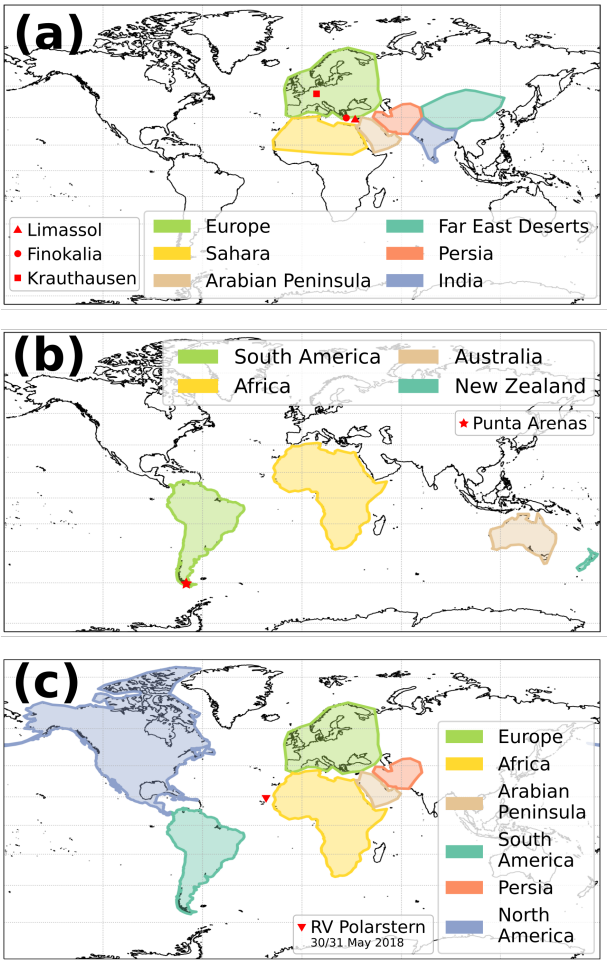

Figure 3. The customly defined geographical areas for Limassol, Finokalia, Krauthausen (all a)~~and~~ , Punta Arenas (b) and the Atlantic transit (c). Locations of the sites are also marked in the respective map.

To illustrate the temporal evolution, successive airmass source profiles can be shown one after ~~each other~~another. This visualization condenses the 4D history of a multitude of trajectories (or thousands of particle positions) to a quickly understandable summary, which ~~closely resembles the~~ structures information on airmass source similar into a time-height cross section~~as~~ . Such a format is usually obtained from vertically or nadir pointed active ground-based remote sensing observations (e.g., Fig. 4).

3 Polly^{XT} lidar observations

The airmass source estimate is used to interpret observations conducted with the Polly^{XT} lidar (Engelmann et al., 2016). Polly^{XT} is equipped with backscatter-channels at 1064, 532 and 355 nm as well Raman- and depolarization-channels at the

shorter two wavelengths. The optical properties are derived using the automated PollyNET retrieval (Baars et al., 2016, 2017; Yin and Baars, 2020) and manual analysis of single profiles. One product of ~~this~~ the PollyNET retrieval is the quasi backscatter coefficient, where the attenuated backscatter is corrected for molecular extinction. ~~Details~~ For this approach, the background, range, and deadtime corrected lidar profiles are normalized by the so called lidar calibration parameter (also sometimes called lidar constant even though it is no constant) which is derived from Raman or Klett retrievals (see Baars et al., 2016) . This normalization gives the attenuated backscatter coefficient from ground (note that for the same atmospheric scene, the attenuated backscatter measured from ground is different to the one measured from space, as it is not corrected for attenuation by molecules and particles). The molecular contribution to the atmospheric backscattering and extinction can be calculated from pressure and temperature profiles, the attenuated backscatter coefficient is corrected for the molecular scattering. Furthermore, an assumption of a fixed lidar ratio is applied on the attenuated backscatter corrected for molecular contribution to account for a first guess of the particulate attenuation. This procedure gives the quasi particle backscatter coefficient which is a good proxy for the real particle backscatter coefficient that cannot yet be obtained at high-temporal resolution for all atmospheric scenes. More details are covered in Baars et al. (2017).

Polly^{XT} was deployed to various field campaigns and longer term measurements during the last 15 years (Baars et al., 2016). A broad variety of meteorological conditions and aerosol regimes was covered. The multi-wavelength observations of Polly^{XT} contain unique fingerprints of the observed aerosol types from different source regions (Illingworth et al., 2015).

In the following sections 4 and 5, the airmass source attribution will be applied to selected case studies and measurement campaigns, in order to demonstrate its applicability for determination of the airmass source regions and for the estimate of potential observation biases. The case studies are ~~taken~~ chosen from deployments of Polly^{XT} to Limassol (Cyprus, 34.7°N, 33.0°E, 12m a.s.l., October 2016 to March 2018), Punta Arenas (Chile, 53.1°S, 70.9°W, 10m a.s.l., November 2018 and ongoing) and the RV *Polarstern* Atlantic transit 2018 when passing Cabo Verde (18.1°N, 21.3°W to 21.3°N, 20.8°W). The estimate of potential observation biases is done for ~~the campaigns~~two multi-weeks campaigns. One at Krauthausen (Germany, 50.9°N, 6.4°E, 99m a.s.l.~~,~~) taking place for 8 weeks in April/May 2013 ~~) and~~ and the second one at Finokalia (Greece, 35.3°N 25.7°E, 250m a.s.l.~~,~~) for 6.5 weeks in June/July ~~2014).~~ 2014.

4 Application to lidar case studies

4.1 Saharan dust off the coast of West Africa

A lofted layer of dust was observed on 30 and 31 May 2018 by a Polly^{XT} system on board RV *Polarstern* (Strass, 2018), as the ship steamed between Cabo Verde and African mainland (18.1°N, 21.3°W to 21.3°N, 20.8°W) on her transit north from Punta Arenas (Chile) to Bremerhaven (Germany). A detailed description of the event and optical properties of the observed aerosol were already reported by Yin et al. (2019).

Fig. 4 illustrates the temporal evolution of the observed aerosol plume by means of ~~the~~ time-height cross section of the 1064 nm quasi particle backscatter coefficient for the time period from 30 May 06 UTC to 31 May 06 UTC. Yin et al. (2019) ~~discussed in detail the time and height period of the observation which is marked by a horizontal orange bar~~ already discussed

this case, especially the period from 16 to 17 UTC (their Fig. 14). Optical parameters from the Raman analysis during the following night from 22 to 23 UTC are shown in Fig. ~~4 (their Fig. 14~~5 (period marked in Fig. 4 (a) with a horizontal orange bar). According to the optical properties ~~they~~ Yin et al. argued that the lowest $1\,\mathrm{km}$ was dominated by marine particles and a certain contribution from European continental aerosol. Patchy, liquid clouds were observed at boundary layer top, especially around 09 and 19 UTC. At larger heights, between 1.8 and $5.2\,\mathrm{km}$ height, a Saharan dust plume with extinction values as large as $700\,\mathrm{Mm^{-1}}$ was present. Lidar ratios were $60\,\mathrm{sr}$ and partlicle linear depolarization ratios at $532\,\mathrm{nm}$ of 0.35. Low Ångström between the lower two wavelengths is consistent with (Veselovskii et al., 2016; Rittmeister et al., 2017). Yin et al. (2019) corroborate their findings by ensemble calculations of HYSPLIT backward trajectories for selected arrival heights and times. However, this way of presentation is rather selective, as information for different heights and times can hardly be shown. This is where the benefit of the continuous airmass source estimate becomes evident. Fig. 6 presents the results of the airmass source estimate for the land surface classification and geographical areas for both, the HYSPLIT (Fig. 6 a,c) and the FLEXPART simulations (Fig. 6, b,d). The estimates based on HYSPLIT and FLEXPART show a good general agreement. The heights and times of certain surface types and geographical regions agree qualitatively. Before 12 UTC on 30 May 2018, FLEXPART derived a lower residence time from barren and grassland or 'Africa', respectively. With respect to Fig. 4, this seems to be reasonable as the layer was rather faint at the beginning of the shown measurement period. Besides this difference, both the HYSPLIT and FLEXPART approaches provide a concise picture of the likely source regions of the observed aerosol. Below $1.5\,\mathrm{km}$ height, the airmass was marine dominated with a small contribution of European grass/cropland. At heights between 2 and $4\,\mathrm{km}$, barren areas from Africa are the main source, but a considerable fraction is also attributed to African grass/cropland and Savanna. This finding is supporting the observations presented by Yin et al. (2019) who already ~~discuss~~ discussed that there was likely a small non-dust fraction in the upper layer, as the particle depolarization ratio profile was not constant at all heights. A potential reason for the observed discrepancy of the observations from pure-dust conditions could be the presence of wildfire smoke stemming from the crop/grassland and savanna. In comparison to the lidar observations, the top of the layer was slightly underestimated by the airmass source estimate. The temporal extent is also fully captured. Variability of backscatter within the layer is not represented by the airmass source estimate, because the strength of dust mobilization is ~~only~~ insufficiently parametrized by the reception height. However, the airmass transport is correctly covered by both estimates. Interestingly, the airmass source estimation for this case provides some added value information with respect to the lidar observations. As both HYSPLIT and FLEXPART approaches indicate, North-American air masses were present in the upper troposphere during the time of the observation, which however had too low aerosol load for being detectable by the Polly$^{\mathrm{XT}}$ lidar.

4.2 Saharan and Arabian dust at Limassol, Cyprus

On ~~the~~ 14 September 2017 an upper-level short-wave trough moved eastward from the Aegean Sea towards Cyprus. Above $1\,\mathrm{km}$ height, the wind turned from South-West to South during the course of the day with velocities ranging ~~from~~ between $5-15\,\mathrm{m\,s^{-1}}$, whereas below, wind velocity was lower and direction more variable.

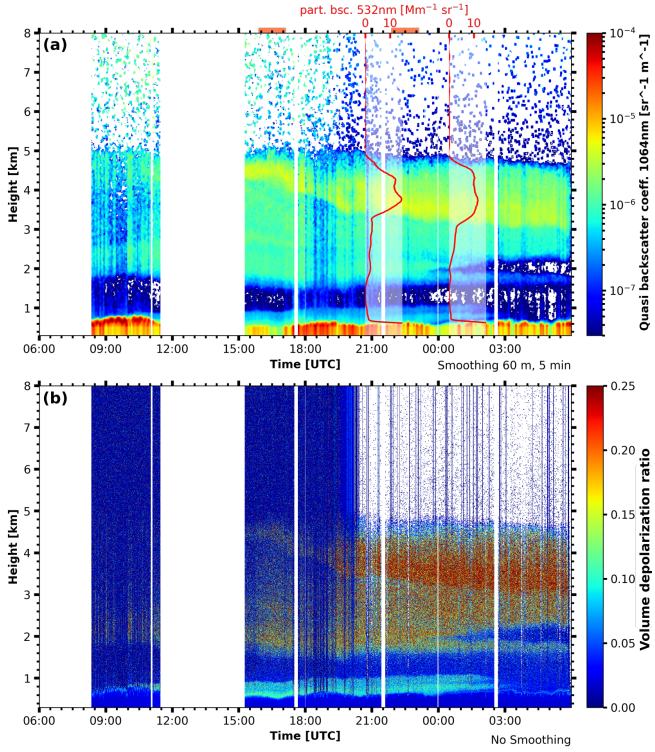

Figure 4. (a) Quasi particle backscatter coefficient at 1064 nm observed by Polly^{XT} on board Polarstern close to Cabo Verde on the 30 and 31 May 2018. Moving average smoothing of 8 range bins (60 m) and 10 temporal bins (5 minutes) was applied. The red overlays show the Klett derived particle backscatter coefficient from the automated algorithm at 532 nm. The time period of manual analysis (see text) is marked by a horizontal orange bar. (b) Volume depolarization ratio at 532 nm for the same period. No smoothing was applied.

The time-height cross-section of quasi particle backscatter observed by Polly^{XT} at Limassol shows two pronounced aerosol layers above the boundary layer (Fig. 7)~~)~~. The first layer was observed between 1 and 2 km height from 0 to 9 UTC and a second, thicker layer after 3 UTC. Until the night, this layer increases in thickness from bases at 3 and tops at 4.5 km height to bases at 1.2 and tops at 6.5 km height. The boundary layer itself is also laden with aerosols and shows significant backscatter below 1 km height.

The optical parameters of the aerosol plume were analyzed for ~~one period in the morning between~~ two periods, 02:59 ~~and -~~ 04:02 UTC ~~and one in the evening between~~ in the morning and 21:~~41 and 22~~41-22:39 UTC in the evening (periods marked in Fig. 7 (a) with horizontal orange bars). The profiles from the morning period (Fig. 8) show for the lower layer at 1.8 km height particle depolarization ratios of 0.25 (355 and 532 nm), low Ångström values and lidar ratios ~~of~~ around 40 sr (355 and 532 nm). These optical parameters and their independence of wavelength are typical for aerosol mixtures with a high dust fraction. Extinction in this layer peaks at 72 Mm^{-1} (355 and 532 nm). The second layer above 2.5 km height has particle backscatter values of less than 2 $Mm^{-1}\,sr^{-1}$ (at 355 nm) and 0.5 $Mm^{-1}\,sr^{-1}$ (at 532 nm). Ångström values are slightly higher

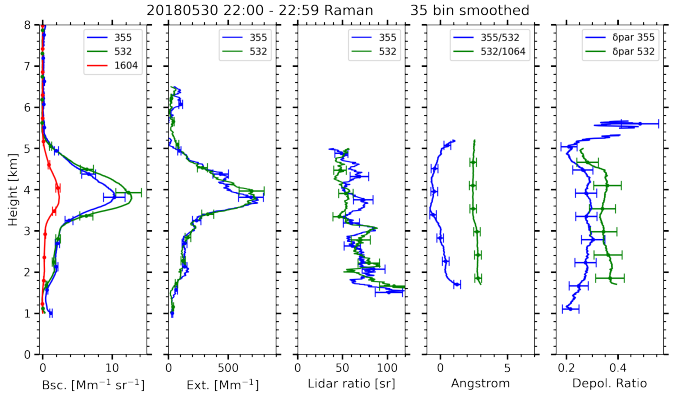

Figure 5. ~~Airmass source estimate from 06 UTC~~ Profiles of optical properties on the 30 ~~to 06 UTC on the 31~~ May 2018 ~~for the land surface classification (a, b)~~ between 22:00 and 22:59 UTC manually derived with the ~~named geographical areas (b, d) based on HYSPLIT (a, c) and FLEXPART~~ Raman method. A vertical smoothing of 35 bins (~~b, d~~262.5 m) was applied.

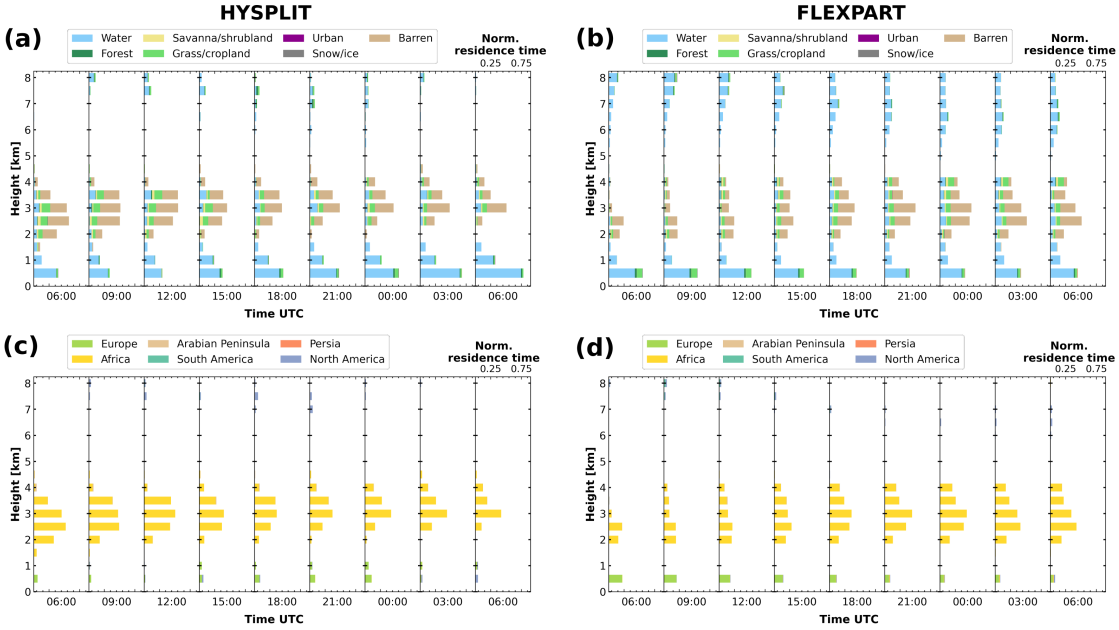

Figure 6. Airmass source estimate from 06 UTC on the 30 to 06 UTC on the 31 May 2018 for the land surface classification (a, b) and the named geographical areas (b, d) based on HYSPLIT ensemble trajectories (a, c) and FLEXPART particle positions (b, d).

than in the lower layer, varying between 1 and 2. The particle depolarization ratios at both, 355 and 532 nm wavelength, are between 0.05 and 0.10. This upper layer during the morning is already the leading edge of the second plume, that increased

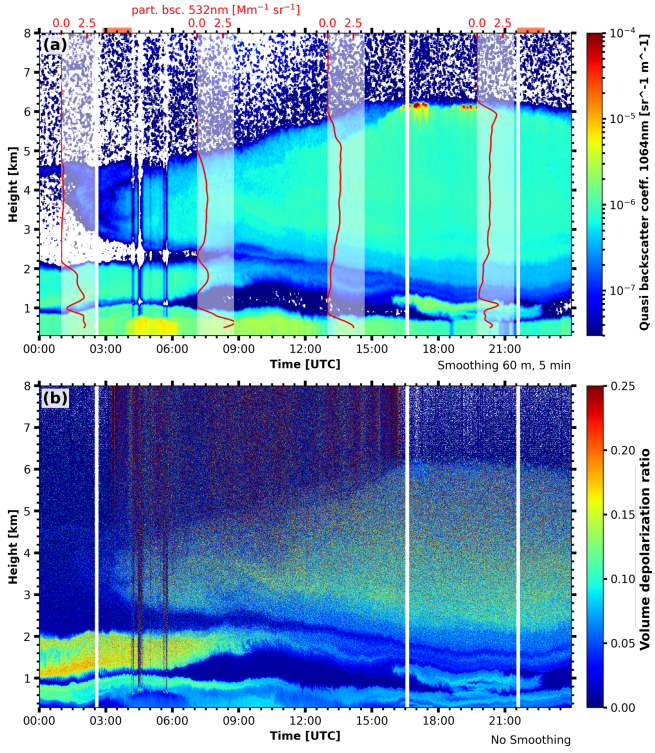

Figure 7. (a) Quasi particle backscatter coefficient at 1064 nm observed by Polly^{XT} at Limassol on the 14 September 2017. Moving average smoothing of 8 range bins (60 m) and 10 temporal bins (5 minutes) was applied. The red overlays show the Klett derived particle backscatter coefficient at 532 nm. The time periods of manual analysis (Fig. 8 and 9) are marked by horizontal orange bars. (b) Volume depolarization ratio at 532 nm for the same period. No smoothing was applied.

in thickness during the day (both geometrically and optical). As shown in Fig. 7 (b), the volume depolarization ratio increased only slowly during the averaging period.

During the evening (Fig. 9), the upper layer extended from 1.3 to 6 km height and shows homogeneous and mostly wavelength-independent optical properties throughout ~~it's depth~~. Particle depolarization ratios were between 0.10 and 0.15, with 532 nm values slightly higher than at 355 nm. Lidar ratios in that layer were 35 sr, typical for ~~middle east dust (Mamouri et al., 2013; Nisantzi et al., 20~~ ~~and~~ Middle East dust (Mamouri et al., 2013; Nisantzi et al., 2015), while the particle depolarization ratio hints towards a mixture of mineral dust and anthropogenic pollution (e.g. Tesche et al., 2009).

The airmass source estimate (Fig. 10) identifies transport from barren-ground-influenced air from the 'Sahara' until 9 UTC. Later, corresponding to the change in wind direction, the source for the air aloft is identified as 'Arabian Peninsula', but still the barren class. Below 1 km height, a mixture of surfaces was observed, originating mostly form 'Europe'. Comparing the source estimate based on HYSPLIT (Fig. 10 a, c) with the one from FLEXPART (Fig. 10 b, d), both models agree qualitatively well again. While the general transition was captured by the source estimate, the leading edge of the 'Arabian Peninsula' plume was

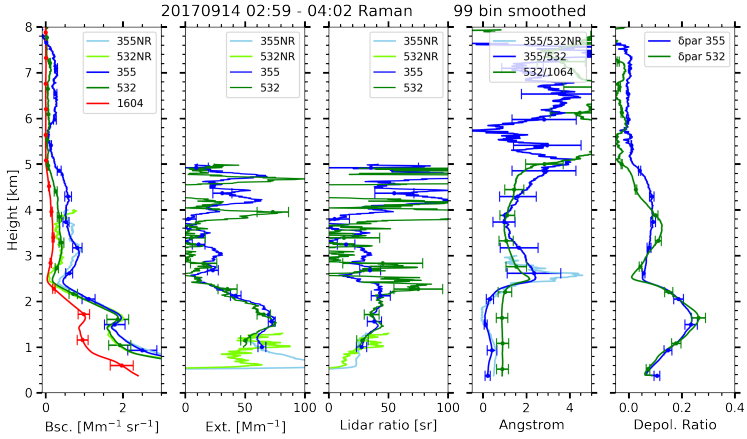

Figure 8. Profiles of optical properties on the 14 September 2017 between 02:59 and 04:02 UTC manually derived with the Raman method. A smoothing ~~length~~ of 99 range bins (742.5 m) was applied. The abbreviation NR marks profiles observed with the larger field-of-view near-range telescope.

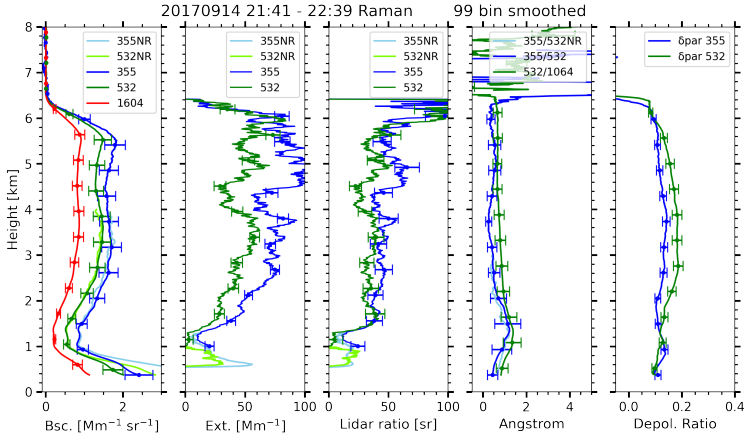

Figure 9. Profiles of optical properties on the 14 September 2017 between 21:41 and 22:39 UTC manually derived with the Raman method. A smoothing ~~length~~ of 99 range bins (742.5 m) was applied. The abbreviation NR marks profiles observed with the larger field-of-view near-range telescope.

observed over Limassol earlier than indicated. The increase in thickness of this plume is represented in the source estimate as well.

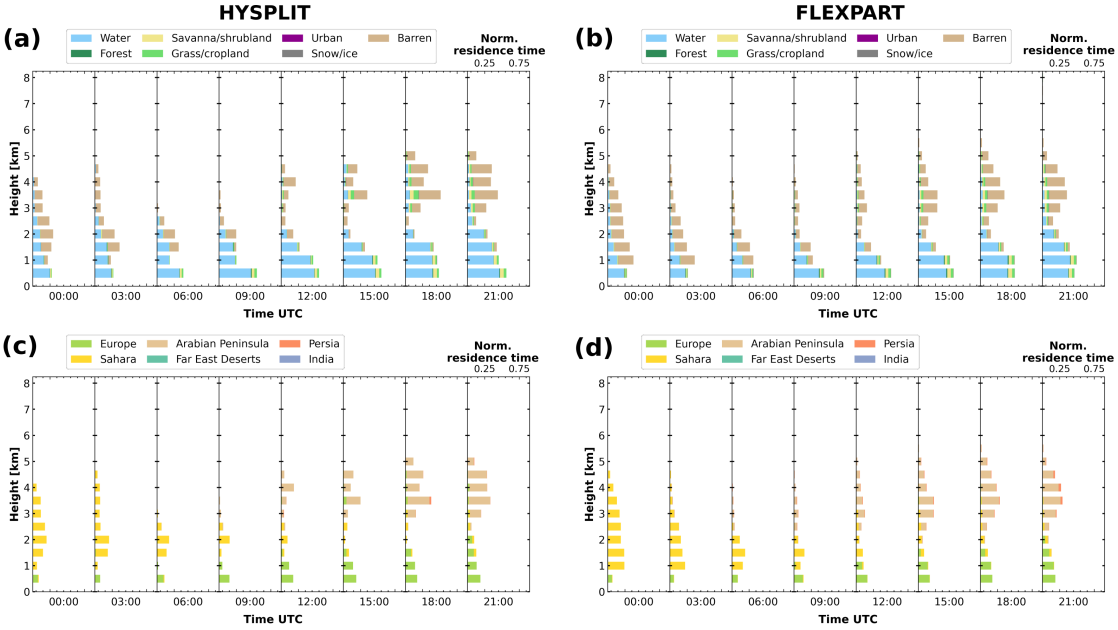

Figure 10. Airmass source estimate on the 14 September 2017 for the land surface classification (a, b) and the named geographical areas (b, d) based on HYSPLIT ensemble trajectories (a, c) and FLEXPART particle positions (b, d).

4.3 Biomass burning aerosol at Punta Arenas, Chile

Punta Arenas is located in a region where the atmosphere is known to be clean and one of the least affected by anthropogenic influences (Hamilton et al., 2014). Nevertheless, events of aerosol long-range transport ~~also~~ occur occasionally (Foth et al., 2019; Floutsi et al., 2020). Due to the large distance of Punta Arenas from aerosol source regions, an attribution of observed aerosol events is in general rather complicated~~at this site~~. The application of airmass source estimate for the characterization of ~~one~~ an aerosol long-range transport event is presented in here. An upper-level ridge was located off the Chilean coast on 20 May 2019, which supported also a surface high pressure system. At Punta Arenas the flow was zonal throughout the troposphere. Within that flow long-range transport from across the Pacific Ocean occurred.

In the Polly$^{\mathrm{XT}}$ observations from 20 May 2019 a layer of increased backscatter is present from 2 UTC to roughly 10 UTC. This layer extends from $3\,\mathrm{km}$ to above $6\,\mathrm{km}$ height (Fig. 11). From 14 to 18 UTC a low-level liquid cloud was observed at $1.5\,\mathrm{km}$ height. The cloud was optically thick enough to significantly attenuate the laser beam, causing lack of signal above the clouds top. Occasional cirrus clouds did also enhance the backscatter in the free troppshere, e.g. at 12 UTC between 4 and $5\,\mathrm{km}$. The values of particle backscatter were peaking at $0.3\,\mathrm{Mm^{-1}\,sr^{-1}}$ (Fig. 12), which are significantly lower values than reported for the prior cases. In the period analyzed, extinction values were approximately $15\,\mathrm{Mm^{-1}}$ giving lidar ratios well above $50\,\mathrm{sr}$ and rather low linear particle depolarization ratios. Altogether these optical parameters agree with prior findings of wildfire smoke in the troposphere (Tesche et al., 2011; Burton et al., 2012; Groß et al., 2013; Veselovskii et al., 2015).

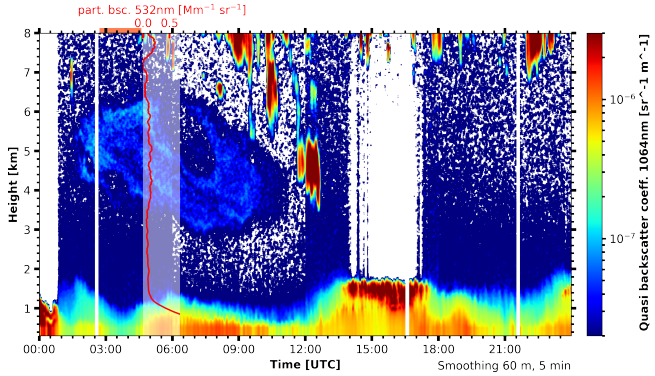

Figure 11. Quasi particle backscatter coefficient at 1064 nm observed by Polly^{XT} at Punta Arenas on the 20 May 2019. Moving average smoothing of 8 range bins (60 m) and 10 temporal bins (5 minutes) was applied. The red overlay shows the Klett derived particle backscatter coefficient at 532 nm. The time period of manual analysis (Fig. 12) is marked by a horizontal orange bar.

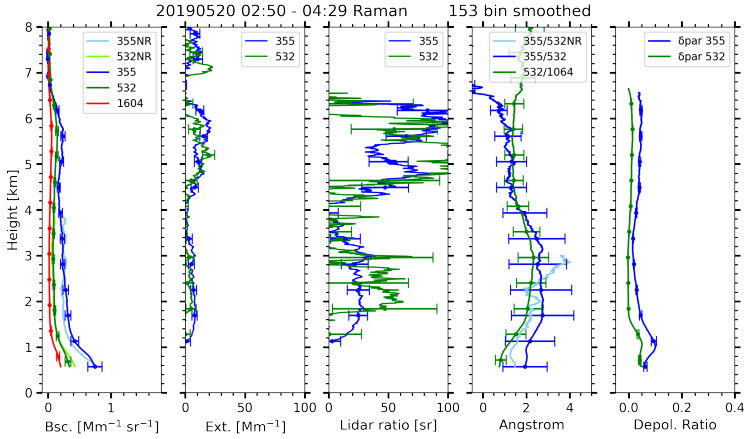

Figure 12. Profiles of optical properties on the 20 May 2019 between 02:50 and 04:30 UTC manually derived with the Raman method. A smoothing ~~length~~ of range 153 bins (1147.5 m) was applied. The abbreviation NR marks profiles observed with the larger field-of-view near-range telescope.

The airmass ~~soruce~~ source estimate is also able to capture this faint aerosol layer. Fig. 13 shows, that airmasses form 225 'Australia' were present between 3 and 9 UTC from 3 to 6 km height. In terms of land cover class these airmasses were characterized by savanna/shrubland and grass. Wildfires were active in south-western Australia between 10 and 16 May 2019, which is also the region, where the backward simulations end (Fig. A1). Apart from the described period, the airmasses were solely influenced by the Southern Ocean (i.e. the water class). FLEXPART simulations (Fig. 13 b, d) agree with the HYSPLIT results, however the computed temporal extend and the residence times are slightly longer for the latter. Hence, the airmass 230 source scheme is also capable of capturing aerosol transport at hemispheric (i.e. more than 10000 km) scales.

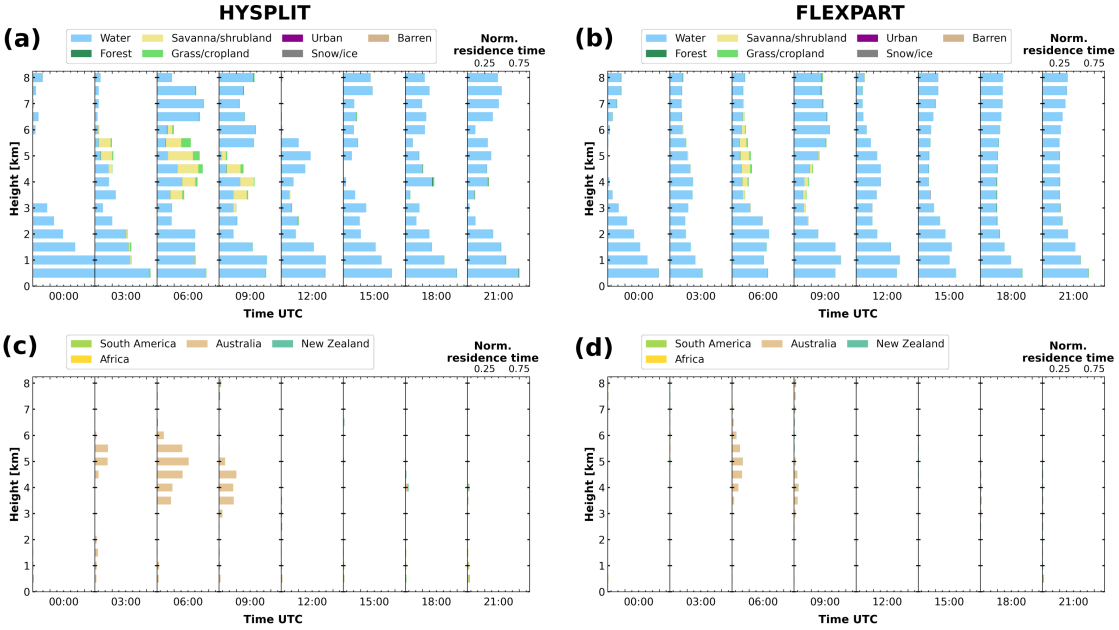

Figure 13. Airmass source estimate on the 20 May 2019 for the land surface classification (a, b) and the named geographical areas (b, d) based on HYSPLIT ensemble trajectories (a, c) and FLEXPART particle positions (b, d).

5 Assessing potential observation biases

Vertically resolved aerosol statistics are prone to observations biases, as they usually depend on cloud-free conditions. When clouds or precipitation are present, no aerosol properties can be obtained from optical techniques. However, respective statistics, for example, obtained from lidar observations provide key quantities for the determination of the environmental conditions at a certain site (Matthias et al., 2004; Winker et al., 2013; Baars et al., 2016). It is therefore an open question whether the data from suitable (cloud-free) measurement periods are representative for the full observational period. Chances are given that cloudy conditions are related to certain air masses which would stay unidentified in the lidar-based statistics of aerosol optical properties. One way to assess this bias is to compare the airmass residence time statistics of the full observational period with the one subsampled to the times when aerosol information is available.

Applied to lidar data, the automatically analyzed profiles of particle backscatter at $532\,\mathrm{nm}$ from Baars et al. (2016) are used. In their work, the raw profiles are grouped into 30-minute chunks, ~~are~~ cloud screened, averaged and analyzed by either the Klett or the Raman method, if signal-to-noise ratio is high enough and a reference height could be set. All profiles that pass a basic quality control are then included into the backscatter statistics. Obviously, this statistic will only be intermittent, due to overcast cloud conditions or interruptions in the measurement. Subsampling the airmass source statistics is done by selecting only the airmass source profiles that are temporally close to a valid lidar profile. A time-threshold of $1.5\,\mathrm{h}$ is used for the

following statistics. However, covering representative airmass conditions is only a necessary condition, not a sufficient one to obtain a representative aerosol statistics.

~~Exemplary, the~~ Polly^{XT} observations at Krauthausen (Germany, April/May 2013) and Finokalia (Greece, June/July 2014) are used here. At Finokalia 940 profiles could be analyzed with the Klett method. Hence, the particle backscatter statistics covers 457.7 h, which is ~~38 %~~ 42 % of the campaign duration. The statistics of particle backscatter is shown in Fig. 14 (a). For the Krauthausen deployment 315 profiles could be analyzed with the Klett method, covering 154.2 h or 11 % of the campaign. Fig. 15 (a) shows the particle backscatter statistics.

Profiles of airmass source for the Finokalia deployment are shown in Fig. 14 (b, c). Again with a reception height threshold of 2 km. The summed residence time of subsampled profiles is divided by the fraction of time covered to make them comparable to the full residence time. Most dominant land surface categories are water, barren and grass-/cropland. The residence time of airmasses ~~originating over~~ from barren ground shows a pronounced maximum between 2 and 6 km height. The residence time of all other categories decreases monotonically. Airmasses from urban and snow or ice covered areas are 10-100 times less frequent, than the other categories.

In terms of geographical areas (Fig. 14 c), 'Europe' is the most dominant source up to 3 km and again above 9 km height. Between 3 and 6 km height the 'Sahara' is the most dominant airmass source. During the campaign period, no airmasses ~~form~~ from the 'Arabian Peninsula', that fulfilled the < 2 km criterion were transported to Finokalia.

The dominant sources are well covered by the lidar profiles in terms of land surface, only the barren class is subsampled by a factor of 10 above 6.5 km height (Fig. 14 b). This agrees to the Sahara also being subsampled above that height. Airmasses originating over 'Europe' were also subsampled at heights above 5 km. An undersampling of potentially aerosol laden airmasses by the lidar statistics will cause the backscatter statistics to be biased low.

During the Krauthausen campaign airmasses originating over water were the most frequent ones, followed by grass-/cropland, forest, shrubland and barren (Fig. 15 b). Again the residence times of the barren class show a distinct peak between 6 and 8 km height. Airmasses form the 'Sahara' area agree with the barren class (Fig. 15 c). As expected, 'Europe' is the dominant airmass source in the lowest 6 km height, but due to increasing residence times with height for the 'Sahara' source, both are equally frequent in the upper troposphere. In the lidar observations, 'Europe' is potentially undersampled by 70 % between 1 and 10 km height, which is consistent with the grass/cropland and forest class also being undersampled. Barren land surfaces and 'Sahara' are oversampled by approximately 20 % up to 7 km height. In the lowermost 2 km height the land surface classes urban and snow/ice also contribute to the airmass mixture and are slightly oversampled.

6 Discussion and Conclusions

In this study we propose an easy to use method for a continuous, height-resolved automated airmass source estimate. By the combination of airmass transport modeling with geographical information, the dimensionality can be reduced and straightforward visualizations accelerate the interpretation of airmass origin. The airmass source estimate can be used to assist (profiling) aerosol observations, as aerosol load and characteristics are strongly controlled by surface properties and atmospheric trans-

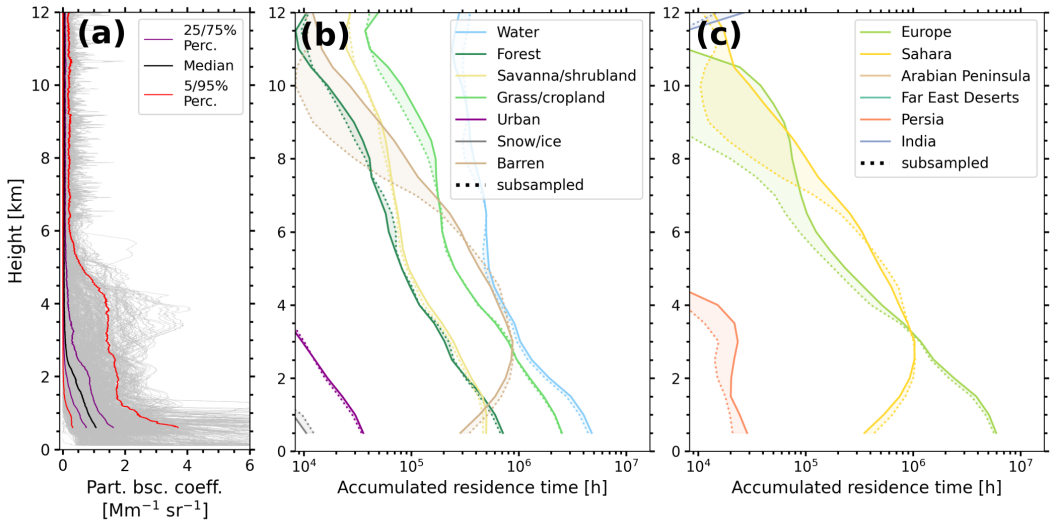

Figure 14. Statistics of particle backscatter coefficient (a, as in Baars et al., 2016) and airmass source estimate based on FLEXPART particle positions for the Finokalia campaign of Polly^{XT} in June and July 2014. The land surface classification (b) and the named geographical areas (c) are shown for the full duration (solid) and subsampled only for the periods with available lidar data (dotted). The subsampled residence times are divided by the fraction of time covered. The reception height threshold is 2 km.

port. Three case studies illustrated the applicability at different sites and under different large scale flow conditions It was also shown how the source estimate supports the interpretation of lidar case studies and how potential observation biases can be investigated for longer term campaigns.

The major ~~constrains~~ constraints of the proposed method are discussed in the following. While the airmass transport itself is generally covered well by trajectory models or LPDMs, the linkage to aerosol properties has to be done with care. Firstly, the reception height is modeled by using the mixing depth of the input fields or fixed values for all surfaces and aerosol particles, where differences could be expected for ~~example for~~ dust, smoke or wildfire smoke. Nevertheless~~for a first estimate~~, the assumption for a general reception height might be valid and can be improved in future. The 2 km height used in this work were also reported by other studies (e.g. for wildfires Val Martin et al., 2018) and seem to be applicable over wide ranges of climates and meteorological conditions. Summarizing, a high residence time over a certain class is only a necessary, not a sufficient condition for aerosol load of an air parcel.

Secondly, aerosol particles might be removed by (wet) deposition between the source and observation site. Currently, such processes are not sufficiently reproduced in trajectory models or LPDMs, as they require detailed representation of aerosol microphysics and precipitation amount. Some improvements in this regard incorporated in the most recent version of FLEXPART (Pisso et al., 2019). However, deposition changes only the aerosol load of an air parcel, not the airmass source itself. Judging from the airmass source residence times alone, this process cannot be distinguished from cases where no emission happened in

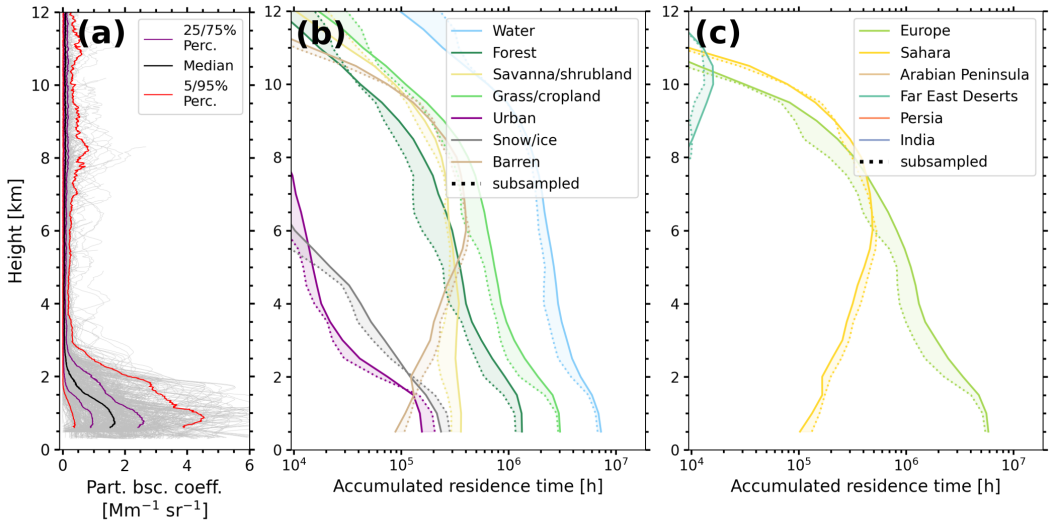

Figure 15. Statistics of particle backscatter coefficient (a, as in Baars et al., 2016) and airmass source estimate based on FLEXPART particle positions for the Krauthausen campaign of Polly^{XT} in April and May 2013. The land surface classification (b) and the named geographical areas (c) are shown for the full duration (solid) and subsampled only for the periods with available lidar data (dotted). The subsampled residence times are divided by the fraction of time covered. The reception height threshold is 2 km.

the first place. These questions could be addressed in future with a ~~fully fledged~~ full-fledged aerosol transport model that also includes a tracer of airmass origin similar to the scheme shown here.

Some uncertainty is caused by the turbulent nature of the transport. For HYSPLIT a first estimate for the uncertainty of a single parcel location is 20 % of the distance from the trajectories origin (Stohl, 1998). Hence, for HYSPLIT a 27-member ensemble was used, to attribute for this uncertainty. Compared to HYSPLIT, the LPDM FLEXPART allows for a more realistic representation to turbulent transport, as well as a better sampling, when using hundreds or thousands of particles. However, a qualitatively good agreement between the both simulations suggests, that the presented airmass source estimate is rather robust considering uncertainty in the models.

In summary, the described compromises are necessary to get a continuous, height-resolved automated and airmass source estimate. The ~~proved~~ provided source code allows to use FLEXPART particle positions and HYSPLIT trajectories as an input. User-defined named geographical areas can be easily added. The runtime ~~enviroment~~ environment is provided as a docker container, including FLEXPART v10.4. With that setup one day of airmass source estimate with the resolution used in this study can be processed in less than an hour on a standard desktop computer (2.1 GHz processor, 4 GB RAM, single-threaded).

Long-term datasets of profiling aerosol observations, such as collected in the network of EARLINET (Pappalardo et al., 2014) are potential further use cases of such an automated airmass source estimate. The methodology could also be adaped to exisiting and future space-borne lidar observations, e.g. CALIPSO (Winker et al., 2009), AEOLUS (Reitebuch, 2012) or EarthCARE (Illingworth et al., 2015). A first estimate of airmass source could be used to constrain retrievals of optical parameters by

narrowing the assumed lidar ratio and guide subsequent aerosol typing. But, simulating enough air parcels with sufficient along-track resolution might require further development.

With respect to typing, downstream products such as estimates of concentration of cloud condensation nuclei or ice nucleating particles will benefit by the airmass source estimate. Either being used on space-borne or ground-based observations. Also further synergy between lidar target categorizations, such as Baars et al. (2017) and the source estimate remain subject to further investigation.

Apart from the shown applications, ~~this approached~~ the presented methodology can be utilized to ~~asses~~ assess profiles of airmass source when planning field campaigns. Questions on where, when or how long to measure in order to capture a certain mix of aerosol scenarios can easily be answered. In future the proposed method can be extended by further source maps, for example by dust source maps derived by the approach of Feuerstein and Schepanski (2018) or temporally varying information on wildfires as well as snow and ice cover or biological productivity.

Code and data availability. The processing software "trace_airmass_source" as used for this publication is available under Radenz (2021). The most recent version is available via GitHub: https://github.com/martin-rdz/trace_airmass_source (last access: 14.01.2021). A Docker configuration is provied for a straightforward replication of the programming environment, including all dependencies. Meteorological fields for the backward simulations were obtained from ARL Archive and NOAA (2000). The data for the fire radiative power map is available at Giglio (2000). The analysed Polly$^{\mathrm{XT}}$ and airmass source data is available on request.

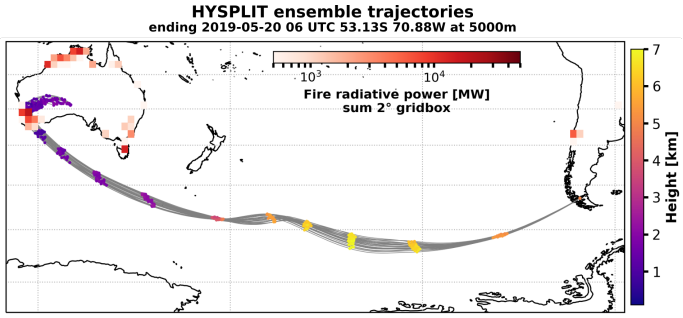

Figure A1. HYSPLIT ensemble backward trajectories ending above Punta Arenas on the 20 May 2019 06 UTC at 5 km height together with the MODIS derived fire radiative power (Giglio, 2000). Dots along the trajectories indicate the height of the air parcel in 12 hour intervals. MODIS derived fire radiative power of fires between 10 and 16 May 2019 is gridded to 2°.

Author contributions. MR developed the algorithm and drafted the manuscript. PS, JB supported the implementation and supervised the work. HB, AF and YZ analyzed the lidar data. All authors jointly contributed to the manuscript and the scientific discussion.

Competing interests. The authors declare that they have no conflict of interest.

Acknowledgements. The research leading to these results has received funding from the European Union's Horizon 2020 research and innovation programme under grant agreement no. 654109 (ACTRIS), the European Union Seventh Framework Programme (FP7/2007–2013) under grant agreement no. 603445 (BACCHUS). We acknowledge funding from the Federal Ministry of Education and Research in Germany (BMBF) through the research program "High Definition Clouds and Precipitation for Climate Prediction – HD(CP)2" (grant nos. 01LK1503F,01LK1502I, 01LK1209C, and 01LK1212C). We thank the Alfred Wegener Institute and R/V Polarstern crew and captain for their support (AWI_PS113_00). Many improvements of the Polly instruments, both, in terms of hard and software were triggered by the fruitful discussions and network activities within EARLINET (Pappalardo et al., 2014).

References

ARL Archive: GDAS1 dataset, https://www.ready.noaa.gov/gdas1.php, 2019 (last accessed: 11.11.2019).

Ashbaugh, L. L.: A Statistical Trajectory Technique for Determining Air Pollution Source Regions, Journal of the Air Pollution Control Association, 33, 1096–1098, https://doi.org/10.1080/00022470.1983.10465702, 1983.

Ashbaugh, L. L., Malm, W. C., and Sadeh, W. Z.: A residence time probability analysis of sulfur concentrations at grand Canyon National Park, Atmospheric Environment (1967), 19, 1263 – 1270, https://doi.org/10.1016/0004-6981(85)90256-2, 1985.

Baars, H., Kanitz, T., Engelmann, R., Althausen, D., Heese, B., Komppula, M., Preißler, J., Tesche, M., Ansmann, A., Wandinger, U., Lim, J.-H., Ahn, J. Y., Stachlewska, I. S., Amiridis, V., Marinou, E., Seifert, P., Hofer, J., Skupin, A., Schneider, F., Bohlmann, S., Foth, A., Bley, S., Pfüller, A., Giannakaki, E., Lihavainen, H., Viisanen, Y., Hooda, R. K., Pereira, S. N., Bortoli, D., Wagner, F., Mattis, I., Janicka, L., Markowicz, K. M., Achtert, P., Artaxo, P., Pauliquevis, T., Souza, R. A. F., Sharma, V. P., van Zyl, P. G., Beukes, J. P., Sun, J., Rohwer, E. G., Deng, R., Mamouri, R.-E., and Zamorano, F.: An overview of the first decade of Polly^{NET}: an emerging network of automated Raman-polarization lidars for continuous aerosol profiling, Atmospheric Chemistry and Physics, 16, 5111–5137, https://doi.org/10.5194/acp-16-5111-2016, 2016.

Baars, H., Seifert, P., Engelmann, R., and Wandinger, U.: Target categorization of aerosol and clouds by continuous multiwavelength-polarization lidar measurements, Atmospheric Measurement Techniques, 10, 3175–3201, https://doi.org/10.5194/amt-10-3175-2017, 2017.

Broxton, P. D., Zeng, X., Sulla-Menashe, D., and Troch, P. A.: A Global Land Cover Climatology Using MODIS Data, Journal of Applied Meteorology and Climatology, 53, 1593–1605, https://doi.org/10.1175/JAMC-D-13-0270.1, 2014.

Burton, S. P., Ferrare, R. A., Hostetler, C. A., Hair, J. W., Rogers, R. R., Obland, M. D., Butler, C. F., Cook, A. L., Harper, D. B., and Froyd, K. D.: Aerosol classification using airborne High Spectral Resolution Lidar measurements – methodology and examples, Atmospheric Measurement Techniques, 5, 73–98, https://doi.org/10.5194/amt-5-73-2012, 2012.

Dipu, S., Quaas, J., Wolke, R., Stoll, J., Mühlbauer, A., Sourdeval, O., Salzmann, M., Heinold, B., and Tegen, I.: Implementation of aerosol–cloud interactions in the regional atmosphere–aerosol model COSMO-MUSCAT(5.0) and evaluation using satellite data, Geoscientific Model Development, 10, 2231–2246, https://doi.org/10.5194/gmd-10-2231-2017, 2017.

Draxler, R. R.: Evaluation of an Ensemble Dispersion Calculation, Journal of Applied Meteorology, 42, 308–317, https://doi.org/10.1175/1520-0450(2003)042<0308:EOAEDC>2.0.CO;2, 2003.

Engelmann, R., Kanitz, T., Baars, H., Heese, B., Althausen, D., Skupin, A., Wandinger, U., Komppula, M., Stachlewska, I. S., Amiridis, V., Marinou, E., Mattis, I., Linné, H., and Ansmann, A.: The automated multiwavelength Raman polarization and water-vapor lidar Polly^{XT}: the neXT generation, Atmospheric Measurement Techniques, 9, 1767–1784, https://doi.org/10.5194/amt-9-1767-2016, 2016.

Escudero, M., Stein, A., Draxler, R., Querol, X., Alastuey, A., Castillo, S., and Avila, A.: Source apportionment for African dust outbreaks over the Western Mediterranean using the HYSPLIT model, Atmospheric Research, 99, 518 – 527, https://doi.org/10.1016/j.atmosres.2010.12.002, 2011.

Feuerstein, S. and Schepanski, K.: Identification of Dust Sources in a Saharan Dust Hot-Spot and Their Implementation in a Dust-Emission Model, Remote Sensing, 11, 4, https://doi.org/10.3390/rs11010004, 2018.

Fleming, Z. L., Monks, P. S., and Manning, A. J.: Review: Untangling the influence of air-mass history in interpreting observed atmospheric composition, Atmospheric Research, 104-105, 1 – 39, https://doi.org/https://doi.org/10.1016/j.atmosres.2011.09.009, 2012.

Flemming, J., Benedetti, A., Inness, A., Engelen, R. J., Jones, L., Huijnen, V., Remy, S., Parrington, M., Suttie, M., Bozzo, A., Peuch, V.-H., Akritidis, D., and Katragkou, E.: The CAMS interim Reanalysis of Carbon Monoxide, Ozone and Aerosol for 2003–2015, Atmospheric Chemistry and Physics, 17, 1945–1983, https://doi.org/10.5194/acp-17-1945-2017, 2017.

Floutsi, A. A., Baars, H., Radenz, M., Haarig, M., Yin, Z., Seifert, P., Jimenez, C., Wandinger, U., Engelmann, R., Barja, B., Zamorano, F., and Ansmann, A.: Biomass burning aerosols in the southern hemispheric midlatitudes as observed with a multiwavelength polarization Raman lidar, Atmospheric Chemistry and Physics Discussions, 2020, 1–27, https://doi.org/10.5194/acp-2020-453, https://www.atmos-chem-phys-discuss.net/acp-2020-453/, 2020.

Foth, A., Kanitz, T., Engelmann, R., Baars, H., Radenz, M., Seifert, P., Barja, B., Fromm, M., Kalesse, H., and Ansmann, A.: Vertical aerosol distribution in the southern hemispheric midlatitudes as observed with lidar in Punta Arenas, Chile (53.2° S and 70.9° W), during ALPACA, Atmospheric Chemistry and Physics, 19, 6217–6233, https://doi.org/10.5194/acp-19-6217-2019, 2019.

Friedl, M., McIver, D., Hodges, J., Zhang, X., Muchoney, D., Strahler, A., Woodcock, C., Gopal, S., Schneider, A., Cooper, A., Baccini, A., Gao, F., and Schaaf, C.: Global land cover mapping from MODIS: algorithms and early results, Remote Sensing of Environment, 83, 287–302, https://doi.org/https://doi.org/10.1016/S0034-4257(02)00078-0, 2002.

Giglio, L.: MODIS Thermal Anomalies/Fire Products, https://doi.org/10.5067/FIRMS/MODIS/MCD14ML, https://earthdata.nasa.gov/earth-observation-data/near-real-time/firms/mcd14ml, 2000.

Groß, S., Esselborn, M., Weinzierl, B., Wirth, M., Fix, A., and Petzold, A.: Aerosol classification by airborne high spectral resolution lidar observations, Atmospheric Chemistry and Physics, 13, 2487–2505, https://doi.org/10.5194/acp-13-2487-2013, 2013.

Haarig, M., Ansmann, A., Gasteiger, J., Kandler, K., Althausen, D., Baars, H., Radenz, M., and Farrell, D. A.: Dry versus wet marine particle optical properties: RH dependence of depolarization ratio, backscatter, and extinction from multiwavelength lidar measurements during SALTRACE, Atmospheric Chemistry and Physics, pp. 14 199–14 217, https://doi.org/10.5194/acp-17-14199-2017, https://www.atmos-chem-phys.net/17/14199/2017/, 2017.

Hamilton, D. S., Lee, L. A., Pringle, K. J., Reddington, C. L., Spracklen, D. V., and Carslaw, K. S.: Occurrence of pristine aerosol environments on a polluted planet, Proceedings of the National Academy of Sciences, 111, 18 466–18 471, https://doi.org/10.1073/pnas.1415440111, 2014.

Heintzenberg, J., Birmili, W., Seifert, P., Panov, A., Chi, X., and Andreae, M. O.: Mapping the aerosol over Eurasia from the Zotino Tall Tower, Tellus B: Chemical and Physical Meteorology, 65, 20 062, https://doi.org/10.3402/tellusb.v65i0.20062, 2013.

Illingworth, A. J., Barker, H. W., Beljaars, A., Ceccaldi, M., Chepfer, H., Clerbaux, N., Cole, J., Delanoë, J., Domenech, C., Donovan, D. P., Fukuda, S., Hirakata, M., Hogan, R. J., Huenerbein, A., Kollias, P., Kubota, T., Nakajima, T., Nakajima, T. Y., Nishizawa, T., Ohno, Y., Okamoto, H., Oki, R., Sato, K., Satoh, M., Shephard, M. W., Velázquez-Blázquez, A., Wandinger, U., Wehr, T., and van Zadelhoff, G.-J.: The EarthCARE Satellite: The Next Step Forward in Global Measurements of Clouds, Aerosols, Precipitation, and Radiation, Bulletin of the American Meteorological Society, 96, 1311–1332, https://doi.org/10.1175/BAMS-D-12-00227.1, 2015.

Kahl, J. D.: A cautionary note on the use of air trajectories in interpreting atmospheric chemistry measurements, Atmospheric Environment. Part A. General Topics, 27, 3037 – 3038, https://doi.org/https://doi.org/10.1016/0960-1686(93)90336-W, arctic air, snow and ice chemistry, 1993.

Lu, Z., Streets, D. G., Zhang, Q., and Wang, S.: A novel back-trajectory analysis of the origin of black carbon transported to the Himalayas and Tibetan Plateau during 1996–2010, Geophysical Research Letters, 39, L01 809, https://doi.org/10.1029/2011GL049903, 2012.

Mamouri, R. E., Ansmann, A., Nisantzi, A., Kokkalis, P., Schwarz, A., and Hadjimitsis, D.: Low Arabian dust extinction-to-backscatter ratio, Geophysical Research Letters, 40, 4762–4766, https://doi.org/10.1002/grl.50898, 2013.

Matthias, V., Balis, D., Bösenberg, J., Eixmann, R., Iarlori, M., Komguem, L., Mattis, I., Papayannis, A., Pappalardo, G., Perrone, M. R., and Wang, X.: Vertical aerosol distribution over Europe: Statistical analysis of Raman lidar data from 10 European Aerosol Research Lidar Network (EARLINET) stations, Journal of Geophysical Research: Atmospheres, 109, D18 201, https://doi.org/10.1029/2004JD004638, 2004.

Mattis, I., Müller, D., Ansmann, A., Wandinger, U., Preißler, J., Seifert, P., and Tesche, M.: Ten years of multiwavelength Raman lidar observations of free-tropospheric aerosol layers over central Europe: Geometrical properties and annual cycle, Journal of Geophysical Research: Atmosphere, 113, https://doi.org/10.1029/2007JD009636, 2008.

Merrill, J. T., Bleck, R., and Avila, L.: Modeling atmospheric transport to the Marshall Islands, Journal of Geophysical Research: Atmospheres, 90, 12 927–12 936, https://doi.org/10.1029/JD090iD07p12927, 1985.

Müller, D., Ansmann, A., Mattis, I., Tesche, M., Wandinger, U., Althausen, D., and Pisani, G.: Aerosol-type-dependent lidar ratios observed with Raman lidar, Journal of Geophysical Research: Atmospheres, 112, https://doi.org/10.1029/2006JD008292, 2007.

Nisantzi, A., Mamouri, R. E., Ansmann, A., Schuster, G. L., and Hadjimitsis, D. G.: Middle East versus Saharan dust extinction-to-backscatter ratios, Atmospheric Chemistry and Physics, 15, 7071–7084, https://doi.org/10.5194/acp-15-7071-2015, 2015.

NOAA, N.: National Centers for Environmental Prediction FNL Operational Model Global Tropospheric Analyses continuing from July 1999, https://doi.org/https://doi.org/10.5065/D6M043C6, https://doi.org/10.5065/D6M043C6, 2000.

Pappalardo, G., Amodeo, A., Apituley, A., Comeron, A., Freudenthaler, V., Linné, H., Ansmann, A., Bösenberg, J., D'Amico, G., Mattis, I., Mona, L., Wandinger, U., Amiridis, V., Alados-Arboledas, L., Nicolae, D., and Wiegner, M.: EARLINET: towards an advanced sustainable European aerosol lidar network, Atmospheric Measurement Techniques, 7, 2389–2409, https://doi.org/10.5194/amt-7-2389-2014, 2014.

Paris, J.-D., Stohl, A., Ciais, P., Nédélec, P., Belan, B. D., Arshinov, M. Y., and Ramonet, M.: Source-receptor relationships for airborne measurements of CO_2, CO and O_3 above Siberia: a cluster-based approach, Atmospheric Chemistry and Physics, 10, 1671–1687, https://doi.org/10.5194/acp-10-1671-2010, 2010.

Pisso, I., Sollum, E., Grythe, H., Kristiansen, N. I., Cassiani, M., Eckhardt, S., Arnold, D., Morton, D., Thompson, R. L., Groot Zwaaftink, C. D., Evangeliou, N., Sodemann, H., Haimberger, L., Henne, S., Brunner, D., Burkhart, J. F., Fouilloux, A., Brioude, J., Philipp, A., Seibert, P., and Stohl, A.: The Lagrangian particle dispersion model FLEXPART version 10.4, Geoscientific Model Development, 12, 4955–4997, https://doi.org/10.5194/gmd-12-4955-2019, 2019.

Polissar, A., Hopke, P., Paatero, P., Kaufmann, Y., Hall, D., Bodhaine, B., Dutton, E., and Harris, J.: The aerosol at Barrow, Alaska: long-term trends and source locations, Atmospheric Environment, 33, 2441 – 2458, https://doi.org/https://doi.org/10.1016/S1352-2310(98)00423-3, 1999.

Radenz, M.: martin-rdz/trace_airmass_source: trace_airmass_source jan2021, https://doi.org/10.5281/zenodo.4438051, 2021.

Reitebuch, O.: The Spaceborne Wind Lidar Mission ADM-Aeolus, pp. 815–827, Springer Berlin Heidelberg, Berlin, Heidelberg, https://doi.org/10.1007/978-3-642-30183-4_49, 2012.

Rieger, D., Bangert, M., Bischoff-Gauss, I., Förstner, J., Lundgren, K., Reinert, D., Schröter, J., Vogel, H., Zängl, G., Ruhnke, R., and Vogel, B.: ICON–ART 1.0 – a new online-coupled model system from the global to regional scale, Geoscientific Model Development, 8, 1659–1676, https://doi.org/10.5194/gmd-8-1659-2015, 2015.

Rittmeister, F., Ansmann, A., Engelmann, R., Skupin, A., Baars, H., Kanitz, T., and Kinne, S.: Profiling of Saharan dust from the Caribbean to western Africa – Part 1: Layering structures and optical properties from shipborne polarization/Raman lidar observations, Atmospheric Chemistry and Physics, 17, 12 963–12 983, https://doi.org/10.5194/acp-17-12963-2017, 2017.

Seibert, P.: Convergence and Accuracy of Numerical Methods for Trajectory Calculations, Journal of Applied Meteorology, 32, 558–566, https://doi.org/10.1175/1520-0450(1993)032<0558:CAAONM>2.0.CO;2, 1993.

Stein, A. F., Draxler, R. R., Rolph, G. D., Stunder, B. J. B., Cohen, M. D., and Ngan, F.: NOAA's HYSPLIT Atmospheric Transport and Dispersion Modeling System, Bulletin of the American Meteorological Society, 96, 2059–2077, https://doi.org/10.1175/BAMS-D-14-00110.1, 2015.

Stohl, A.: Trajectory statistics-A new method to establish source-receptor relationships of air pollutants and its application to the transport of particulate sulfate in Europe, Atmospheric Environment, 30, 579 – 587, https://doi.org/https://doi.org/10.1016/1352-2310(95)00314-2, 1996.

Stohl, A.: Computation, accuracy and applications of trajectories—A review and bibliography, Atmospheric Environment, 32, 947 – 966, https://doi.org/10.1016/S1352-2310(97)00457-3, 1998.

Stohl, A., Wotawa, G., Seibert, P., and Kromp-Kolb, H.: Interpolation Errors in Wind Fields as a Function of Spatial and Temporal Resolution and Their Impact on Different Types of Kinematic Trajectories, Journal of Applied Meteorology, 34, 2149–2165, https://doi.org/10.1175/1520-0450(1995)034<2149:IEIWFA>2.0.CO;2, 1995.

Stohl, A., Eckhardt, S., Forster, C., James, P., Spichtinger, N., and Seibert, P.: A replacement for simple back trajectory calculations in the interpretation of atmospheric trace substance measurements, Atmospheric Environment, 36, 4635 – 4648, https://doi.org/https://doi.org/10.1016/S1352-2310(02)00416-8, 2002.

Stohl, A., Forster, C., Frank, A., Seibert, P., and Wotawa, G.: Technical note: The Lagrangian particle dispersion model FLEXPART version 6.2, Atmospheric Chemistry and Physics, 5, 2461–2474, https://doi.org/10.5194/acp-5-2461-2005, 2005.

Strass, V. H.: The Expedition PS113 of the Research Vessel POLARSTERN to the Atlantic Ocean in 2018, https://doi.org/10.2312/BzPM_0724_2018, https://www.tib.eu/de/suchen/id/awi%3Adoi%7E10.2312%252FBzPM_0724_2018, 2018.

Tarasova, O. A., Senik, I. A., Sosonkin, M. G., Cui, J., Staehelin, J., and Prévôt, A. S. H.: Surface ozone at the Caucasian site Kislovodsk High Mountain Station and the Swiss Alpine site Jungfraujoch: data analysis and trends (1990–2006), Atmospheric Chemistry and Physics, 9, 4157–4175, https://doi.org/10.5194/acp-9-4157-2009, 2009.

Tesche, M., Ansmann, A., Müller, D., Althausen, D., Engelmann, R., Freudenthaler, V., and Groß, S.: Vertically resolved separation of dust and smoke over Cape Verde using multiwavelength Raman and polarization lidars during Saharan Mineral Dust Experiment 2008, Journal of Geophysical Research: Atmospheres, 114, D13 202, https://doi.org/10.1029/2009JD011862, 2009.

Tesche, M., Gross, S., Ansmann, A., Müller, D., Althausen, D., Freudenthaler, V., and Esselborn, M.: Profiling of Saharan dust and biomass-burning smoke with multiwavelength polarization Raman lidar at Cape Verde, Tellus B: Chemical and Physical Meteorology, 63, 649–676, https://doi.org/10.1111/j.1600-0889.2011.00548.x, 2011.

Val Martin, M., Kahn, R., and Tosca, M.: A Global Analysis of Wildfire Smoke Injection Heights Derived from Space-Based Multi-Angle Imaging, Remote Sensing, 10, 1609, https://doi.org/10.3390/rs10101609, 2018.

Veselovskii, I., Whiteman, D. N., Korenskiy, M., Suvorina, A., Kolgotin, A., Lyapustin, A., Wang, Y., Chin, M., Bian, H., Kucsera, T. L., Pérez-Ramírez, D., and Holben, B.: Characterization of forest fire smoke event near Washington, DC in summer 2013 with multi-wavelength lidar, Atmospheric Chemistry and Physics, 15, 1647–1660, https://doi.org/10.5194/acp-15-1647-2015, 2015.

Veselovskii, I., Goloub, P., Podvin, T., Bovchaliuk, V., Tanre, D., Derimian, Y., Korenskiy, M., and Dubovik, O.: Study of African Dust with Multi-Wavelength Raman Lidar During "Shadow" Campaign in Senegal, EPJ Web of Conferences, 119, 08 003, https://doi.org/10.1051/epjconf/201611908003, 2016.

Wernli, B. H. and Davies, H. C.: A lagrangian-based analysis of extratropical cyclones. I: The method and some applications, Quarterly Journal of the Royal Meteorological Society, 123, 467–489, https://doi.org/10.1002/qj.49712353811, 1997.

Winker, D. M., Vaughan, M. A., Omar, A., Hu, Y., Powell, K. A., Liu, Z., Hunt, W. H., and Young, S. A.: Overview of the CALIPSO Mission and CALIOP Data Processing Algorithms, Journal of Atmospheric and Oceanic Technology, 26, 2310–2323, https://doi.org/10.1175/2009jtecha1281.1, 2009.

Winker, D. M., Tackett, J. L., Getzewich, B. J., Liu, Z., Vaughan, M. A., and Rogers, R. R.: The global 3-D distribution of tropospheric aerosols as characterized by CALIOP, Atmospheric Chemistry and Physics, 13, 3345–3361, https://doi.org/10.5194/acp-13-3345-2013, 2013.

Yin, Z. and Baars, H.: PollyNET/Pollynet_Processing_Chain: Version 2.0, https://doi.org/10.5281/zenodo.3774689, https://doi.org/10.5281/zenodo.3774689, 2020.

Yin, Z., Ansmann, A., Baars, H., Seifert, P., Engelmann, R., Radenz, M., Jimenez, C., Herzog, A., Ohneiser, K., Hanbuch, K., Blarel, L., Goloub, P., Dubois, G., Victori, S., and Maupin, F.: Aerosol measurements with a shipborne Sun–sky–lunar photometer and collocated multiwavelength Raman polarization lidar over the Atlantic Ocean, Atmospheric Measurement Techniques, 12, 5685–5698, https://doi.org/10.5194/amt-12-5685-2019, 2019.